

An empirical zenith wet delay correction model using piecewise height functions

YiBin Yao^{1,2,3}, YuFeng Hu^{1*}

¹*School of Geodesy and Geomatics, Wuhan University, 129 Luoyu Road, Wuhan 430079, China.*

²*Key Laboratory of Geospace Environment and Geodesy, Ministry of Education, Wuhan University,
129 Luoyu Road, Wuhan 430079, China*

³*Collaborative Innovation Center for Geospatial Technology, 129 Luoyu Road, Wuhan 430079,
China*

*Corresponding to: yfhu@whu.edu.cn

Abstract—Tropospheric delay is an important error source in space geodetic techniques. The temporal and spatial variations of the zenith wet delay (ZWD) are very large, and thus limit the accuracy of tropospheric delay modelling. Thus it is worthwhile undertaking research aimed at constructing a precise ZWD model. Based on the analysis of vertical variations of ZWD, we divided the troposphere into three height intervals: below 2 km, 2 km to 5 km, and 5 km to 10 km, and determined the fitting functions for the ZWD within these height intervals. The global empirical ZWD model HZWD, which considers the periodic variations of ZWD with a spatial resolution of $5^\circ \times 5^\circ$, is established using the ECMWF ZWD profiles from 2001 to 2010. Validated by the ECMWF ZWD data in 2015, the precisions of the ZWD estimation in the HZWD model over the three height intervals are improved by 1.4 mm, 0.9 mm, and 1.2 mm, respectively, compared to that of the currently best GPT2w model (23.8 mm, 13.1 mm, and 2.6 mm). The test results from ZWD data from 318 radiosonde stations show that the root mean square (RMS) error in the HZWD model over the three height intervals was reduced by 2% (0.6 mm), 5% (0.9 mm), and 33% (1.7 mm), respectively, compared to the GPT2w model (30.1 mm, 15.8 mm, and 3.5 mm) over the three height intervals. In addition, the spatial and temporal stabilities of the HZWD model are higher than those of GPT2w and UNB3m.

29 ***Index Terms***—Tropospheric delay, zenith wet delay, vertical variations, height dividing,
30 HZWD model.

31

32 **1 Introduction**

33 The radio waves experience propagation delays when passing through the neutral
34 atmosphere (primarily the troposphere), which are known as the tropospheric delays.
35 The tropospheric delay is one of the main error source in space geodetic techniques. In
36 the processing of the space geodetic data, the tropospheric delay along the propagation
37 path is generally expressed as the product of zenith tropospheric delay (ZTD) and
38 mapping function (MF). The ZTD is divided into a zenith hydrostatic delay (ZHD) and
39 a zenith wet delay (ZWD) (Davis *et al.*, 1985), and the ZHD can be accurately
40 determined using pressure observations. Unlike the ZHD, the ZWD is difficult to
41 calculate accurately due to the high spatio-temporal variation in water vapour. Its spatial
42 distribution is characterized with a near-zonal dependency, with values varying from
43 about 2 cm at high latitudes to about 35 cm near the equator (Fernandes *et al.*, 2013).
44 The temporal variation pattern of ZWD is mainly characterized by the seasonal
45 variability including annual and semi-annual components (Jin *et al.*, 2007; Nilsson *et al.*,
46 2008). The high variabilities in ZWD make itself the main factor influencing
47 tropospheric delay correction.

48 Various methods and models are developed to estimate the ZWD. Ray-tracing uses
49 the observations from radiosonde profile (Davis *et al.*, 1985; Niell, 1996) or numerical
50 weather models (Hobiger *et al.*, 2008; Nafisi *et al.*, 2012) to calculate the ZWD. It can
51 provide the most accurate ZWD corrections. Models such as those developed by Bevis
52 *et al.* (1992, 1994) make use of single layer parameters from atmospheric models, such
53 as total column water vapour (TCWV) and temperature. While Stum *et al.* (2011)
54 proposed a model that only uses TCWV. These models provide similar results to the
55 Davis *et al.* (1985) (that uses 3D parameters) but only at the level of the model
56 orography to which the meteorological parameters refer to. As this orography may
57 depart significantly from the actual surface and the vertical variation of the ZWD is not

58 well known, at a different elevation they possess errors associated with the uncertainty
59 in the modelling of the ZWD height variation (Fernandes *et al.*, 2013, 2014; Vieira *et*
60 *al.*, 2018). The traditional Saastamoinen model (1972) and Hopfield model (1971)
61 approximate the ZWD with surface observations as temperature and water vapour
62 pressure observations. Without the information about the vertical distribution of water
63 vapour, the stability and reliability of their ZWD estimates are poor. Moreover, both
64 models are highly dependent on meteorological data. The aforementioned models have
65 the limitations of application in wide area augmentation and real-time navigation and
66 positioning. Therefore, the empirical climatological models were proposed as practical
67 conditions required. The RTCA-MOPS (2016), designed by the US Wide Area
68 Augmentation System (Collins *et al.*, 1996), estimates ZWD by using the latitude band
69 parameters table. The modified RTCA-MOPS model – called UNB3m (Leandro, 2006)
70 – uses relative humidity as a parameter instead of the water vapour pressure to calculate
71 the ZWD, effectively improving the precision of ZWD estimation to 5.5 cm (Möller *et*
72 *al.*, 2014), but the model deviation is increased when the height exceeds 2 km (Leandro,
73 2006). The TropGrid model (Krueger *et al.*, 2004, 2005) provides the meteorological
74 parameters needed to calculate tropospheric delay in the form of $1^\circ \times 1^\circ$ grid. The
75 improved TropGrid2 model (Schüler, 2014) enhances the efficiency of ZWD
76 calculation by directly modelling ZWD with the exponential function. Based on the
77 GPT2 model (Lagler *et al.*, 2013), the GPT2w model (Böhm *et al.*, 2015) adds weighted
78 mean temperature and a vapour pressure decrease factor realised as a global grid to
79 estimate ZWD by using the Askne and Nordius formula (Askne & Nordius, 1987). The
80 GPT2w model has the best precision of ZWD estimation (3.6 cm) compared to other
81 commonly used models (Möller *et al.*, 2014).

82 The water vapour changes rapidly with respect to height, and the trends in water
83 vapour at different heights vary, so the wet delay with direct relation to water vapour
84 has complex spatio-temporal variations in the vertical direction. Kouba (2008)
85 proposed an empirical exponential model to account for the height dependency of ZWD,
86 but it will only be applicable within the height below 1000 m. The aforementioned
87 empirical models are all based on a fixed height (average sea level or surface height)

88 and use only a single decrease factor to describe the variation of water vapour or wet
 89 delay with respect to height, which makes it difficult to allow for the vertical
 90 distribution differences in water vapour (or wet delay) in the upper troposphere. In the
 91 course of aircraft dynamic navigation and positioning, the zenith delay error will result
 92 in two times errors in the station height estimate (Břhm and Schuh, 2013). Thus it is
 93 necessary to correct the wet delay at different heights, which is clearly difficult for the
 94 aforementioned models. Based on the analysis of the characteristics of the ZWD profile,
 95 an empirical ZWD model, named HZWD, is established based on three functions
 96 applicable within corresponding height intervals, and the model precision is verified by
 97 European Centre for Medium-Range Weather Forecast (ECMWF) reanalysis data as
 98 well as radiosonde data.

99

100 **2 Vertical variations of ZWD**

101 ZWD is defined as the integral of the wet refractivity along the vertical profile
 102 above the station:

$$103 \quad ZWD = 10^{-6} \int_H^{\infty} N_w dh = 10^{-6} \int_H^{\infty} (k'_2 \frac{e}{T} + k_3 \frac{e}{T^2}) dh \quad (1)$$

104 In equation (1), N_w is the wet refractivity; e is the water vapour pressure in hPa;
 105 T is the temperature in Kelvin; k'_2 is 22.1 K/hPa and k_3 is 373900 K²/hPa (Bevis *et*
 106 *al.*, 1994). It can be seen from equation (1) that ZWD changes with height, vapour
 107 pressure and temperature. The ZWD will decrease with increasing height due to the
 108 shorter integral length. With the profiles of water vapour pressure and temperature, one
 109 can obtain the accurate ZWD by ray tracing method. However, in practical applications
 110 (*e.g.*, aircraft navigation and positioning, wide area augmentation), we usually use
 111 empirical models for ZWD corrections due to the unavailability of meteorological data
 112 profiles. Therefore, it is necessary to develop an empirical ZWD model with high
 113 precision. The temperature roughly decreases linearly with increasing height in the
 114 troposphere, while the change in water vapour is more variable, so the water vapour is
 115 the main determinant of vertical variation of ZWD. In the following content, we used

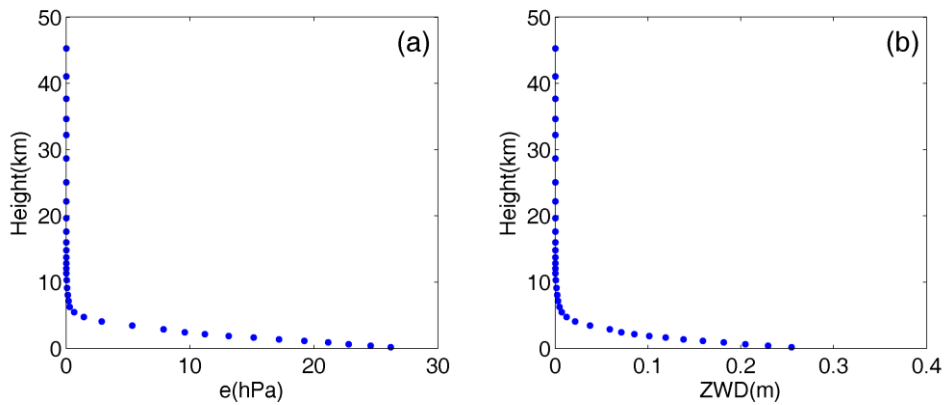
116 the meteorological data profile of ERA-Interim pressure levels provided by ECMWF
 117 to analyse the vertical variation characteristics of ZWD and explore a suitable fitting
 118 function capable of describing the changes in ZWD with respect to height.

119 ERA-Interim can provide data at 0:00, 6:00, 12:00, and 18:00 UTC daily with a
 120 spatial resolution of not more than $0.75^\circ \times 0.75^\circ$ and 37 pressure levels (Dee *et al.*,
 121 2011). The highest level data come from a height of approximately 50 km, covering
 122 almost the entire troposphere and stratosphere. We used the temperature, the
 123 geopotential height, and the specific humidity provided by the ERA-Interim pressure
 124 levels data, and the discretised form of equation (1), to calculate the ZWD for each level
 125 height (Böhm and Schuh, 2013):

$$126 \quad \begin{cases} e_i = q_i \times P_i / (0.622 + 0.378 \times q_i) \\ N_{w_i} = k'_2 \frac{e_i}{T_i} + k_3 \frac{e_i}{T_i^2} \\ ZWD = 10^{-6} \sum_i^{36} \frac{N_{w_i} + N_{w_{i+1}}}{2} \cdot (h_{i+1} - h_i) \end{cases} \quad (2)$$

127 In equation (2), q is the specific humidity in g/g; P is the pressure in hPa; k'_2 and k_3
 128 are empirical constants same as equation (1); h is the geopotential height in meters.
 129 From equation (2), we can see that the ZWD at specific level height is the sum of the
 130 ZWD portions in all layers above the specific level height. Figure 1 shows the water
 131 vapour pressure and ZWD profiles at a grid point (0° N, 0° E) at 12:00 UTC on 1
 132 January, 2010. From Figure 1, it can be seen that the downward trend in the water
 133 vapour pressure varies significantly with height, and the decrease factor is different
 134 across different height intervals. The changes in ZWD with respect to height are similar
 135 to that of the water vapour pressure with respect to height: the decay is fastest up to a
 136 few kilometres height and slows down with increasing height; the ZWD values are close
 137 to zero after 10 km. Zhao *et al.* (2014) showed that about 50% of the water vapour
 138 content is concentrated within 1.5 km of the surface and less than 10% of the water
 139 vapour content remains above 5 km, leading to different ZWD decay rates within
 140 different height intervals. These results are basically consistent with our experiment

141 results. Further, the derivative of the ZWD with respect to height (*i.e.*, ZWD vertical
 142 gradient) is analyzed to better understand the characteristic of the ZWD vertical
 143 distributions. Figure 2a shows the variation of ZWD vertical gradients with respect to
 144 height at the same grid point to Figure 1. From Figure 2a, it can be seen that the trends
 145 in ZWD vertical gradients at different height intervals are clearly different. Specifically,
 146 the linear fit of the ZWD gradients with height below 2 km shows a great agreement
 147 with an R square value of 0.99 (Figure 2b). Thus we can come to a conclusion: ZWD
 148 gradients roughly change linearly below 2 km; and from 2 km to 5 km, and 5 km to 10
 149 km, the ZWD gradients vary non-linearly.

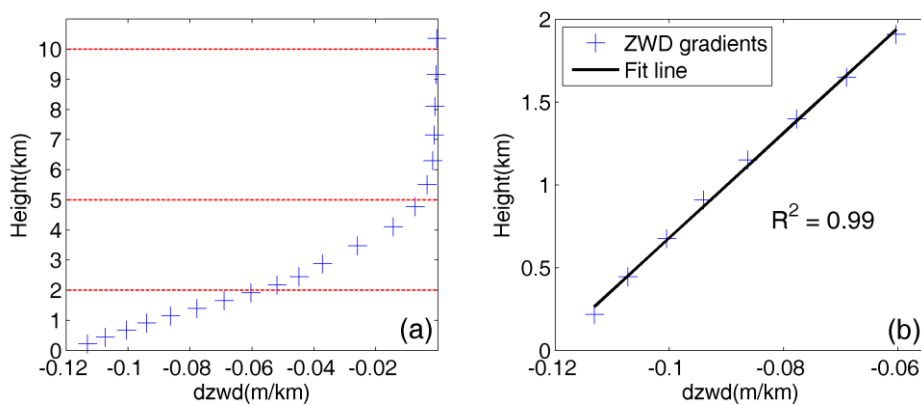


150

151 Figure 1 Water vapour pressure profile (a) and ZWD profile (b) at a grid point (0 °N, 0 °E) at

152

12:00 UTC on 1 January, 2010.



153

154 Figure 2 ZWD vertical gradients profile (a) and linear fit with height below 2 km (b) at a grid

155

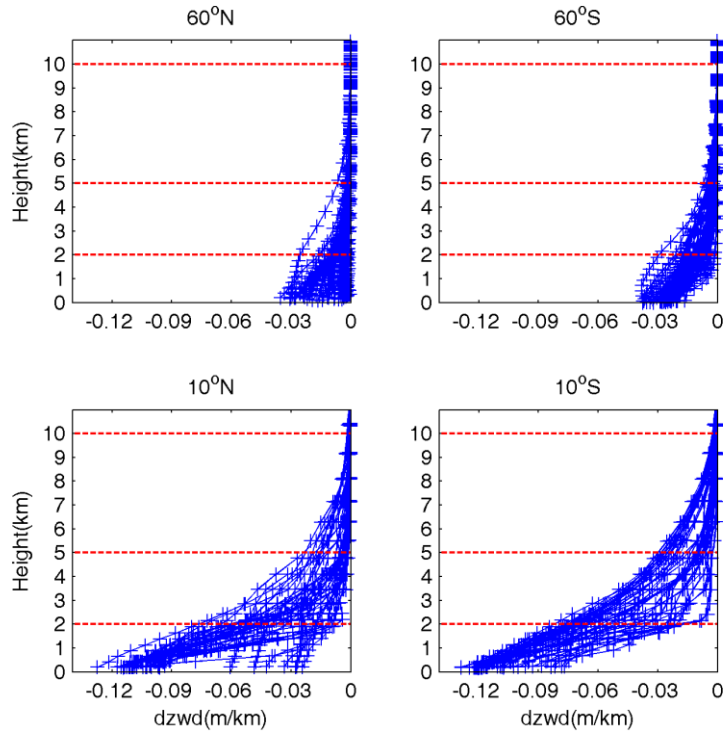
point (0 °N, 0 °E) at 12:00 UTC on 1 January, 2010.

156

157

Figure 3 shows the ZWD vertical gradients with respect to height at grid points in
 different latitude bands. Figure 4 shows the similar ZWD vertical gradients as Figure 3

158 but for different season. The variations are similar to those in Figure 2a, which show
159 trend changes at about 2 km and 5 km. It is worth noting that the ZWD gradients at low
160 latitudes are much larger and water vapour is more variable than at high latitudes,
161 resulting from the fact that the water vapour at low latitude is more variable. In addition,
162 the ZWD gradient trends in the southern hemisphere are significant. In contrast, the
163 ZWD gradients in the northern hemisphere are slightly complicated with respect to
164 height: the reason for this may be that the southern hemisphere is mostly oceanic while
165 the northern hemisphere has many seacoasts. The terrain complexity in the northern
166 hemisphere contributes to the disturbances in the ZWD gradient in specific areas.
167 According to the vertical variation characteristics of ZWD, we divided the troposphere
168 into three height intervals: below 2 km, 2 km to 5 km, and 5 km to 10 km, and assumed
169 10 km as the empirical tropopause beyond which the ZWD is assumed to be zero. For
170 ZWD fitting with respect to height, TropGrid2 and GPT2w use exponential functions,
171 while some scholars have also used a polynomial to describe the tropospheric delay
172 with respect to height (Song *et al.*, 2011). We used both polynomial and exponential
173 functions to fit the variation trend of the ZWD with respect to height in the three
174 selected intervals, respectively. The results showed that the quadratic polynomial used
175 under 2 km, and exponential functions between 2 km and 5 km, and 5 km to 10 km
176 gave the best fits. The combination of the quadratic polynomial and exponential
177 functions for different height intervals is termed piecewise height functions. Table 1
178 summarises the global fitting statistics of different fit functions, demonstrating the
179 superiority of piecewise height functions to the single polynomial function and single
180 exponential function used for the whole troposphere.

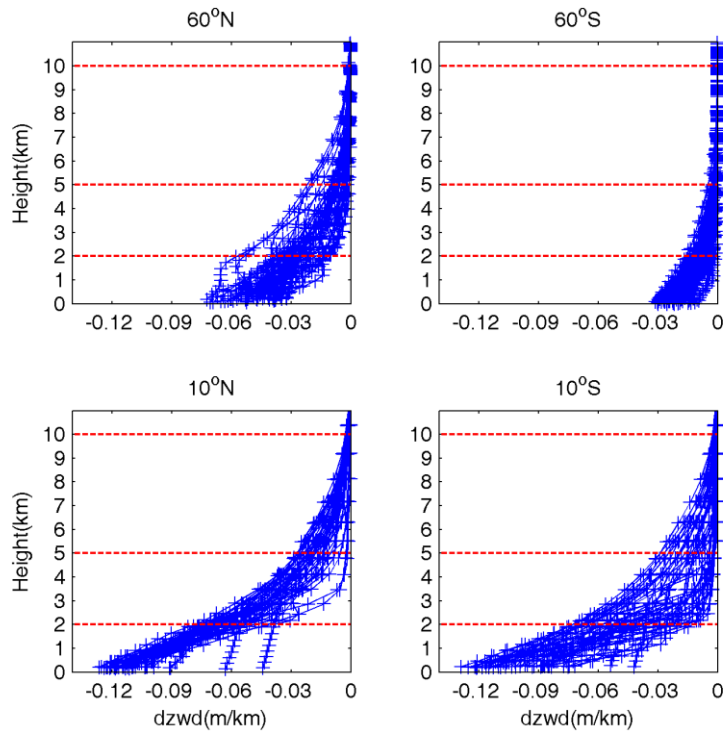


181

182 Figure 3 ZWD gradients profiles at grid points in different latitude bands (12:00 UTC, 1 January,

183

2010).



184

185 Figure 4 ZWD gradients profiles at grid points in different latitude bands (12:00 UTC, 1 July,

186

2010).

187

188 Table 1. Fitting RMS of piecewise height functions, single quadratic polynomial function, and

189

single exponential function (unit: mm).

	< 2 km	2 km to 5 km	5 km to 10 km
Piecewise height functions	0.2	1.0	0.2
Quadratic polynomial	5.9	3.8	6.5
Exponential	2.3	2.2	1.0

190

191 **3 The HZWD model**

192 From the above analysis of ZWD vertical variation and fitting, the piecewise height

193 functions of the proposed HZWD model are:

$$194 \quad ZWD(B, L, H) = \begin{cases} z_1 + a_1 \cdot H + a_2 \cdot H^2 & H < 2000 \text{ m} \\ z_2 \cdot \exp\{\beta_2 \cdot (H - 2000)\} & 2000 \text{ m} \leq H < 5000 \text{ m} \\ z_3 \cdot \exp\{\beta_3 \cdot (H - 5000)\} & 5000 \text{ m} \leq H \leq 10000 \text{ m} \\ 0 & H > 10000 \text{ m} \end{cases} \quad (3)$$

195

In equation (3), B is the latitude in degrees; L is the longitude in degrees; H is the

196

height in meters; function coefficients z_1, z_2 and z_3 can be regarded as the ZWD at

197

the height of 0 km, 2 km and 5 km, respectively. We used the monthly mean profiles of

198

ERA-Interim pressure levels from 2001 to 2010 with a horizontal resolution of $5^\circ \times 5^\circ$

199

for ZWD modelling. The ZWD profiles calculated for each grid point are fitted by

200

equation (3) to obtain the time series of the corresponding function coefficients: $z_1,$

201

 $a_1, a_2, z_2, \beta_2, z_3,$ and β_3 . It is worth noting that the ERA-Interim-derived ZWD

202

data indicate that the averaged ZWD values at the three height intervals (*i.e.*, below 2

203

km, 2 km to 5 km, and 5 km to 10 km) are 0.126 m, 0.0489 m, and 0.0111 m,

204

respectively. Jin *et al.* (2007) found that the tropospheric delay has notable seasonal

205

variations, mainly on annual and semi-annual cycles. Song *et al.* (2011) and Zhao *et al.*

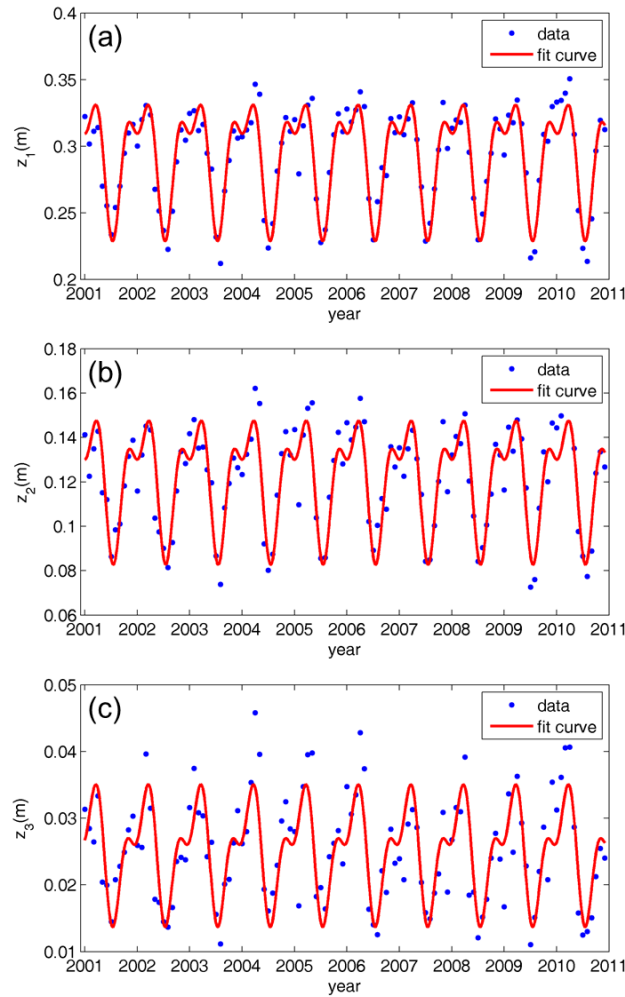
206

(2014) considered the temporal features of function coefficients in their troposphere

207

models. We used the ten-year time series of those coefficients obtained to analyse their

208 temporal variations. Figure 5 shows the time series and cycle fitting results of the
 209 function coefficients z_1 , z_2 , and z_3 at grid point (0°N, 0°E). Figure 5 shows that
 210 the time series of the function coefficients z_1 , z_2 , and z_3 have a significant
 211 characteristic annual cycle, and the semi-annual cycle is small but nevertheless evident.



212

213 Figure 5 Decadal time series and cycle fitting results of function coefficients z_1 (a), z_2 (b), and

214

z_3 (c) at a grid point (0°N, 0°E) from 2001 to 2010.

215

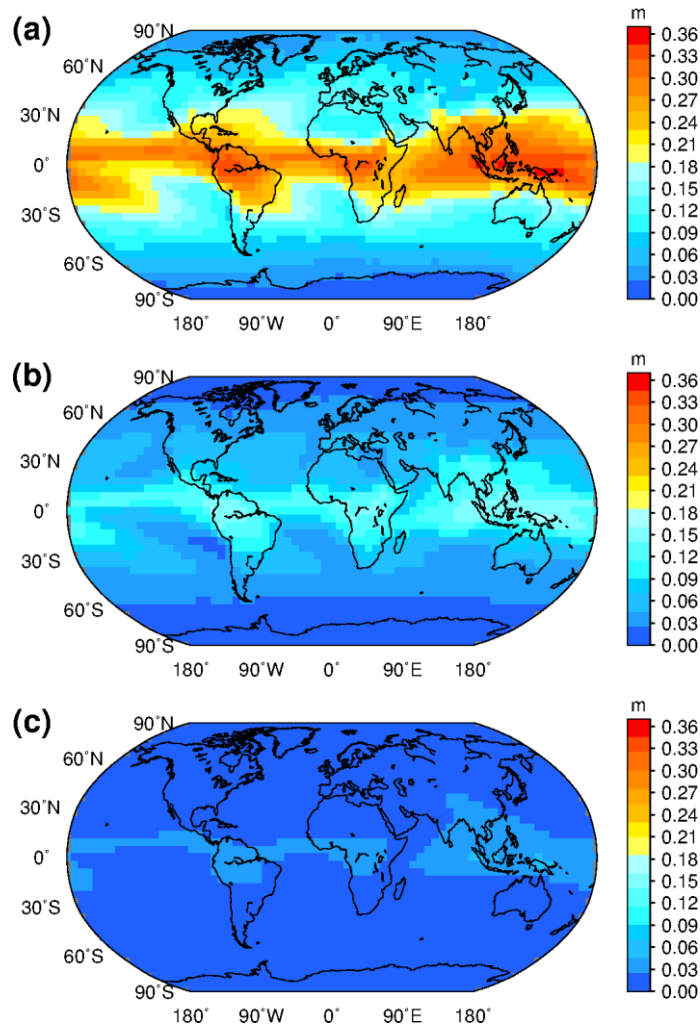
Therefore, taking the annual, and semi-annual cycles into consideration, we used
 216 equation (4) to fit the function coefficients derived from equation (3) to temporal
 217 parameters for each grid point (Böhmer *et al.*, 2015):

$$\begin{aligned}
218 \quad r(t) = & A_0 + A_1 \cos\left(\frac{doy}{365.25} 2\pi\right) + B_1 \sin\left(\frac{doy}{365.25} 2\pi\right) \\
& + A_2 \cos\left(\frac{doy}{365.25} 4\pi\right) + B_2 \sin\left(\frac{doy}{365.25} 4\pi\right)
\end{aligned} \tag{4}$$

219 In equation (4), A_0 is the annual mean; A_1 and B_1 are the annual cycle
220 parameters; A_2 and B_2 are the semi-annual cycle parameters; and *doy* is the day of
221 the year. The fittings show that the annual means, and annual, and semi-annual
222 amplitudes of z_1 , z_2 and z_3 are distinct. For instance, the cycle fitting results at a
223 grid (0 °N, 0 °E) (Figure 5) indicate that the temporal parameters (*i.e.*, $A_0, A_1, B_1, A_2,$
224 and B_2) of z_1 are 0.2911 m, 0.0237 m, 0.0312 m, -0.0006 m, and -0.0227 m,
225 respectively; the temporal parameters of z_2 are 0.1215 m, 0.0118 m, 0.0203 m, 0.0004
226 m, and -0.0146 m, respectively; the temporal parameters of z_3 are 0.0255 m, 0.00031
227 m, 0.0070 m, -0.0019 m, and -0.0044 m, respectively. It should be noted that the fitting
228 results of coefficients a_2 , β_2 , and β_3 show that all their annual means, and annual,
229 and semi-annual amplitudes are small. However, below 2 km, the lack of cycle terms
230 in a_2 would cause centimetre level error in the ZWD estimates, so these terms have
231 been retained. For β_2 and β_3 , ZWD itself is small at heights above 2 km, so the
232 annual mean suffices for a desirable ZWD estimate. The experiment reveals that the
233 loss of accuracy due to the lack of annual and semi-annual terms in β_2 and β_3 for
234 the ZWD estimates is less than 0.1 mm. Therefore, only the annual means are retained
235 for these two coefficients.

236 Figure 6 shows the global distributions of annual means of model coefficients z_1 ,
237 z_2 , and z_3 . From Figure 6 we can see that the extremum of ZWD annual means at 0 m
238 height occur near the equator and the maximum exceeds 0.36 m. The ZWD annual
239 means decrease with increasing latitude. The distributions of ZWD annual means at 2
240 km and 5 km heights are similar to that at 0 m, but the areas with the large values near

241 the equator decrease in extent and the ZWD distributions tend to be uniform, indicating
 242 that the water vapour content near the equator is greater than that in other regions, and
 243 the ZWD value is also larger in low altitude regions. As the height increases, the
 244 difference in water vapour content or ZWD, between the equator and other areas begins
 245 to decrease, but remains significant. Overall, there are some differences in the ZWD
 246 distribution at different heights, and it is necessary to model the spatio-temporal
 247 variations of ZWD at different heights.



248

249 Figure 6 Global distributions of annual means of HZWD model coefficients z_1 (a), z_2 (b),

250

and z_3 (c).

251

252

253

After the fitting processes involving equations (3) and (4), the global ZWD model HZWD, using piecewise height functions, is established. The spatial resolution of the HZWD model is $5^\circ \times 5^\circ$. Each grid point contains 7 primary coefficients: z_1 , a_1 , a_2 ,

254 z_2 , β_2 , z_3 , and β_2 . Among these coefficients, z_1 , z_2 , z_3 , a_1 , and a_2 are further
 255 expressed by equation (4) with 5 temporal parameters, respectively. Therefore, there
 256 are 27 parameters for each grid point and total 68094 parameters for the HZWD model.
 257 As a comparison, the GPT2w model has a number of 77760 parameters, which is 14%
 258 more than that of the HZWD model. It is worth noting that the UNB3m model only has
 259 50 parameters due to its coarse spatio-temporal resolution. When the HZWD model is
 260 applied, the four grid points surrounding the station are determined according to the
 261 horizontal position (latitude and longitude) of the station, and then the model
 262 coefficients of the corresponding height intervals at the four selected points are
 263 calculated according to equation (4). The ZWD of the four grid points are extrapolated
 264 to the station height by using equation (3), and finally the ZWD at the station location
 265 is obtained by using bilinear interpolation. The HZWD model only needs time, latitude,
 266 longitude, and height as input parameters. It can calculate ZWD without meteorological
 267 data, and can provide wet delay correction products for navigation and positioning at
 268 different heights.

269

270 **4 Validation and analysis of the HZWD model**

271 To test the precision of HZWD model and analyse the model correction
 272 performance compared to other troposphere models, we used the ERA-Interim pressure
 273 levels data and radiosonde data from the year 2015 as external data sources, and
 274 compared the results with the commonly used models UNB3m and GPT2w. The
 275 parameters used for the validation are bias and root mean square (RMS) error expressed
 276 as:

$$277 \quad bias = \frac{1}{n} \sum_{i=1}^n (ZWD_i^M - ZWD_i^0) \quad (5)$$

$$278 \quad RMS = \sqrt{\frac{1}{n} \sum_{i=1}^n (ZWD_i^M - ZWD_i^0)^2} \quad (6)$$

279 In equation (5) and (6), ZWD_i^M is the value estimated by the HZWD model
 280 developed in this study and ZWD_i^0 is the reference value.

281 For the UNB3m model, the ZWD at mean sea level (MSL) is first calculated, then

282 a vertical correction is applied to transform the ZWD to the target height. The formulae
 283 are (Leandro *et al.*, 2006):

$$284 \quad \begin{cases} ZWD_0 = 10^{-6} \frac{(T_m k'_2 + k_3) R_d}{g_m (\lambda + 1) - \gamma R_d} \cdot \frac{e_0}{T_0} \\ ZWD = ZWD_0 \left(1 - \frac{\gamma H}{T_0} \right)^{\frac{(\lambda+1)g}{\gamma R_d} - 1} \end{cases} \quad (7)$$

285 where e_0 , T_0 , and ZWD_0 are the water vapour pressure, temperature and ZWD at
 286 MSL, respectively; R_d is the specific gas constant for dry air ($278.054 \text{ J kg}^{-1} \text{ K}^{-1}$); γ
 287 and λ are the temperature lapse rate and water vapour decrease factor, respectively;
 288 g_m is the gravity acceleration at the mass centre of the vertical column of the
 289 atmosphere and can be computed with geodetic latitude φ and height h by:

$$290 \quad g_m = 9.784 \left(1 - 0.00266 \cos 2\varphi - 0.28 \cdot 10^{-6} h \right) \quad (8)$$

291 T_m is the weighted mean temperature computed by:

$$292 \quad T_m = T_0 \left(1 - \frac{\gamma R_d}{g_m (\lambda + 1)} \right) \quad (9)$$

293 For the GPT2w model, the modelled meteorological parameters at the four grid
 294 points surrounding the target location are extrapolated vertically to the desired height,
 295 then the Askne and Nordius formula (10) is used to calculate the wet delays at those
 296 base points: finally the wet delays are interpolated to the observation site in horizontal
 297 direction to get the target ZWD.

$$298 \quad ZWD = 10^{-6} \cdot \left(k'_2 + \frac{k_3}{T_m} \right) \cdot \frac{R_d e}{(\lambda + 1) g_m} \quad (10)$$

299 In GPT2w model, T_m is an empirical parameter modelled with seasonal
 300 components and g_m is simplified to a constant (9.80665 m s^{-2}). It should be noted that
 301 the GPT2w model provides both $1^\circ \times 1^\circ$ and $5^\circ \times 5^\circ$ resolution versions. Since the
 302 horizontal resolution of HZWD model is $5^\circ \times 5^\circ$, we used the GPT2w model with the
 303 same resolution for validation.

304 **4.1 Validation with ECMWF data**

305 Modelling of the HZWD model is based on the monthly mean profiles of ERA-
 306 Interim pressure levels data from 2001 to 2010, while we used the ERA-Interim
 307 pressure levels data with the full time resolution of 6 hours in 2015 for the model
 308 validation. This is to validate the model performance on the daily scale. Regarding the
 309 ZWD profiles calculated from these data as reference values, we calculated the global
 310 annual average bias and RMS error of the ZWD for three models (HZWD, GPT2w, and
 311 UNB3m) within the three height intervals: below 2 km, 2 km to 5 km, and 5 km to
 312 10 km (Table 2).

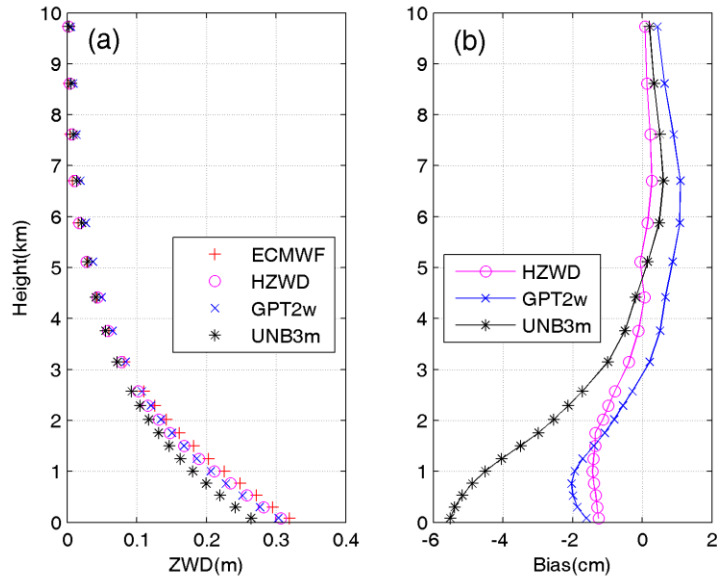
313 Table 2 Error statistics for the three models compared to the 2015 ECMWF data (unit: mm).

	< 2 km		2 km to 5 km		5 km to 10 km	
	bias	RMS	bias	RMS	bias	RMS
HZWD	-2.0	23.8	-1.4	13.1	0.0	2.6
GPT2w	-0.1	25.2	2.5	14.0	2.2	3.8
UNB3m	16.6	41.4	10.9	22.7	3.5	5.8

314 From Table 2, it can be seen that the HZWD model is the most accurate model
 315 across all three intervals, followed by the GPT2w model, and the UNB3m model has
 316 the worst performance. The annual average biases of the HZWD model are lower than
 317 that of the GPT2w model and the UNB3m model except below 2 km. Compared with
 318 the RMS errors in the GPT2w model, those of the HZWD model are decreased by 1.4
 319 mm, 0.9 mm, and 1.2 mm within the three height intervals, corresponding to
 320 improvements of about 6%, 6%, and 32%, respectively. The improvements of HZWD
 321 model over GPT2w model will result in precision improvements of 2.8 mm, 1.8 mm,
 322 and 2.4 mm respectively in height estimates in real-time aircraft positioning. The
 323 correction performance improvement from 5 km to 10 km height is particularly evident.
 324 Figure 7a shows the ECMWF ZWD profile and the ZWD profiles of the three models
 325 at 12:00 UTC on 1 January, 2015 at a representative grid point (0 °N, 20 °E). More
 326 clearly, Figure 7b shows the differences between the ZWD profiles of the three models
 327 and ECMWF ZWD profile at different heights. It can be seen that HZWD is the most

328 stable model, showing the best agreement with the ECMWF ZWD data, which is
 329 superior to both the GPT2w, and the UNB3m, models.

330



331

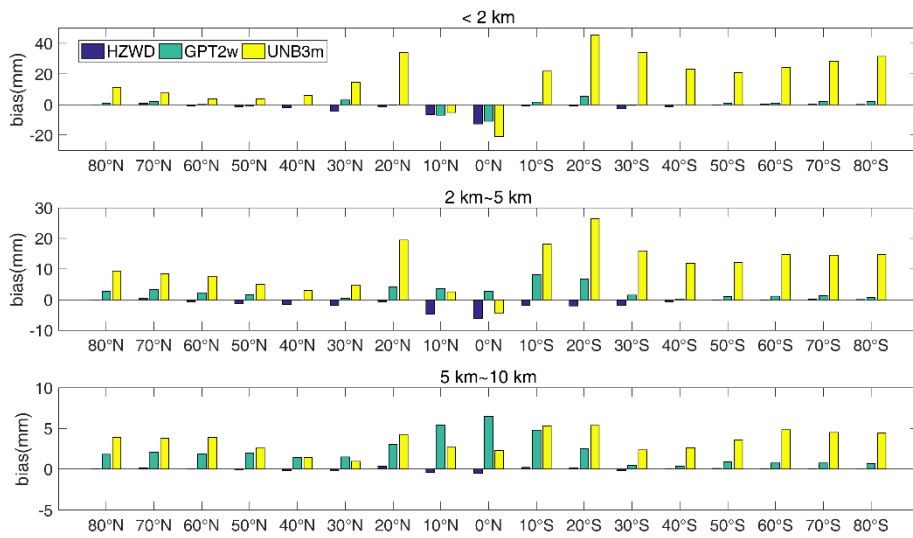
332 Figure 7 The ZWD profiles (a) of ECMWF and the three models (HZWD, GPT2w, and UNB3m)
 333 and corresponding biases (b) at a grid point (0 °N, 20 °E) at 12:00 UTC on 1 January, 2015.

334 The variation of the troposphere has a strong correlation with latitude. To analyse
 335 the correction performances of the three models in different regions around the world,
 336 we calculated the three models' errors in different latitude bands (10 °intervals). Figures
 337 8 and 9 show the correction performances at different latitudes. It can be seen from
 338 Figure 8 that the bias of the UNB3m model is basically positive in the three height
 339 intervals, indicating that its ZWD estimates are relatively large compared to the
 340 ECMWF data. Moreover, the bias in the southern hemisphere is significantly larger than
 341 that in the northern hemisphere, indicating systematic deviations in the southern
 342 hemisphere. Both the GPT2w model and the HZWD model have large biases in the low
 343 latitudes. The biases of the GPT2w model are positive from 2 km to 5 km and 5 km to
 344 10 km height, indicating that the ZWD is overestimated by the GPT2w model with
 345 increasing height. For the HZWD model, the bias in each latitude band is relatively
 346 small with few exceptions, resulting in a global average bias close to zero (see Table 2).

347 Figure 9 shows the RMS errors of the three models. It can be seen from Figure 9
 348 that the precision of HZWD model is significantly better than that of the UNB3m model

349 across the three height intervals and all latitude bands, which is better than GPT2w
350 model in general. The precision of the three models declines with decreasing latitude,
351 because the active change of water vapour in these areas limits the precision of the
352 model. Corresponding to Figure 8, the errors in UNB3m are asymmetric: the main
353 reason for this is that the meteorological parameters of UNB3m are interpolated from
354 the coarse look-up table with a latitude interval of 15° and UNB3m does not consider
355 the longitudinal variations of any meteorological elements. It should be pointed out that
356 the UNB3m model is based on the simple symmetric assumption of the northern and
357 southern hemispheres, and its modelling data source only comes from the atmospheric
358 data collected over North America, which leads to poor precision in the southern
359 hemisphere, especially in the high latitudes thereof.

360 Summarising the distributions of bias and RMS error across different latitude
361 bands, we can see that the HZWD model performs best with the ECMWF data as
362 reference values. Compared with the models GPT2w and UNB3m, the HZWD model
363 basically eliminates systematic error in the 5 km to 10 km height interval and the
364 correction performance is stable at all heights and regions. To investigate the model's
365 performance over time, Figure 10 shows the time series of RMS for the three models at
366 6-hour intervals throughout the year 2015 at grid point (0°N , 20°E). We can see that
367 the HZWD model has the best overall performances within the three height intervals
368 over the year 2015. We noticed the significantly large RMS for all three models across
369 all three height intervals around the day 19 and day 195 of 2015. This can be attributed
370 to the sharp short-term ZWD variations in the equator area. The short-term variations
371 are hardly accounted for by all three models which only consider the seasonal variations
372 of ZWD. Moreover, the GPT2w model has the worst performance from 5 km to 10 km
373 height, which is also identified by Figure 8 and Figure 9.

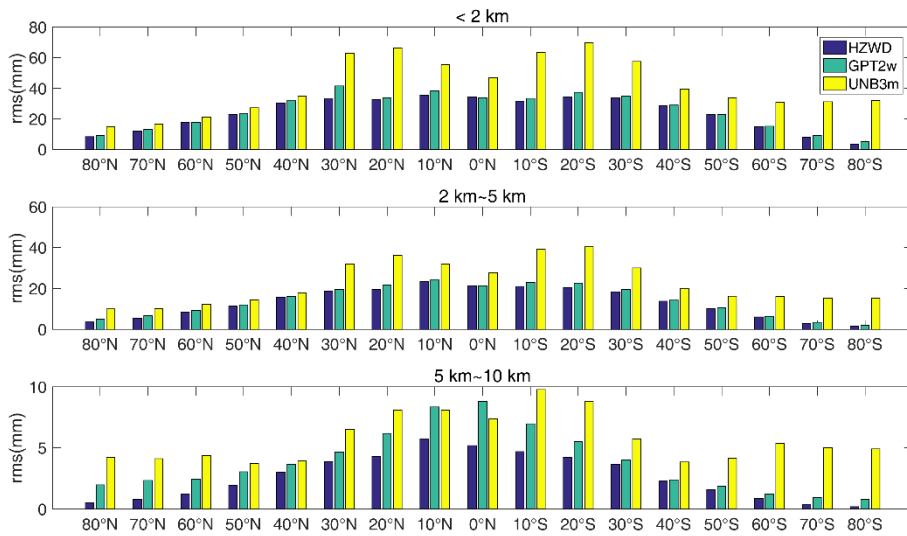


374

375 Figure 8 Bias comparisons between the three models (HZWD, GPT2w, and UNB3m) in different

376

latitude bands over the year 2015.



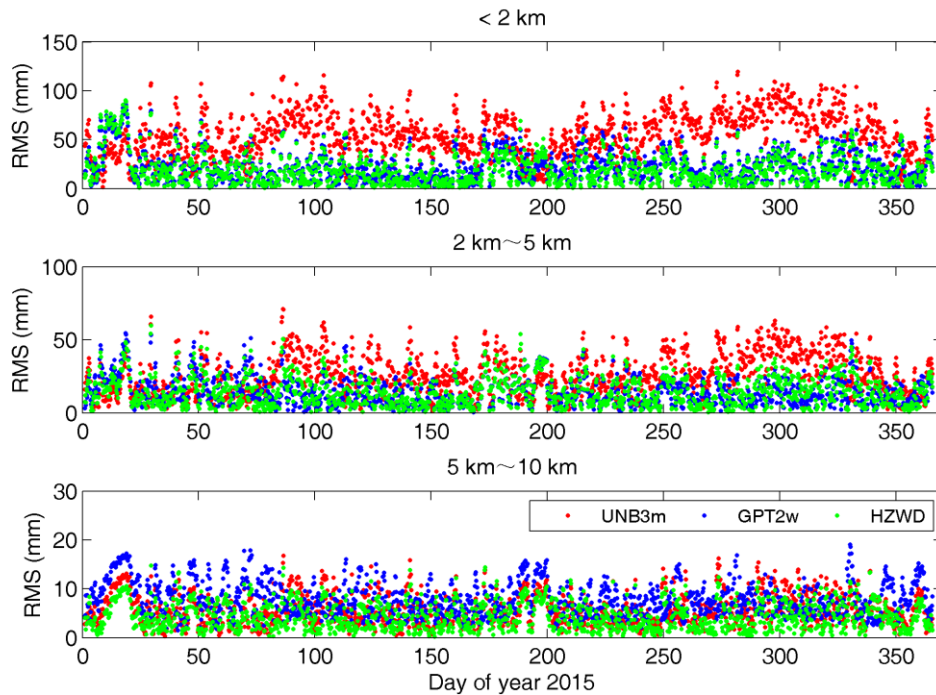
377

378 Figure 9 RMS error comparisons between the three models (HZWD, GPT2w, and UNB3m) in

379

different latitude bands over the year 2015.

380



381

382 Figure 10 RMS errors in ZWD estimates of the three models (HZWD, GPT2w, and UNB3m)

383

compared to the ECMWF data over the year 2015 at grid point (0°N, 20°E).

384

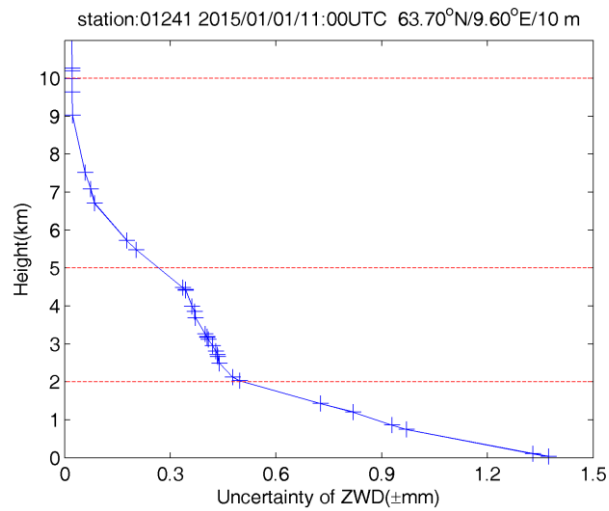
385 4.2 Validation with radiosonde data

386

A radiosonde is used in a sounding technique that regularly releases balloons to collect atmospheric meteorological data at different heights: it can obtain profiles of various meteorological data with high accuracy. At present, the Integrated Global Radiosonde Archive (IGRA) website (<ftp://ftp.ncdc.noaa.gov/pub/data/igra/>) provides free downloads of global radiosonde data. We used radiosonde data from 318 stations collected in 2015 to test the HZWD model. After data pre-processing, the data with gross errors have been removed and a total of 163,671 radiosonde data epochs remained. With the provided profiles of geopotential height, temperature, and water vapour pressure, the data form of the radiosonde data are very similar to the ECMWF pressure level data, thus the radiosonde ZWDs can be calculated using the same method by equation (2). Before the validation, we conducted an assessment of the uncertainty of ZWD derived from radiosonde data. Rozsa (2014) showed that the uncertainty of ZWD is ± 1.5 mm in case of the Vaisala RS-92 radiosondes in Central and Eastern Europe. However, this uncertainty is only valid for the ZWD calculated from the height of

399

400 lowest layer and is limited to Europe area. Using the same uncertainties of radiosonde
 401 meteorological data given by the technical specification of the radiosonde and the
 402 algorithm proposed by Rozsa (2014), we calculated the ZWD uncertainty for all heights
 403 in all radiosonde stations. Figure 11 shows the uncertainty of ZWD with respect to the
 404 height for radiosonde station 01241 located in Orland, Norway (63.70°N/9.60°E/10 m).
 405 We can see that the uncertainty of ZWD is less than ± 1.5 mm near height of 0 m and
 406 decrease quickly with increasing height. The global mean uncertainties of ZWD of all
 407 stations in the three height intervals are ± 1.3 mm, ± 0.7 mm and ± 0.2 mm,
 408 respectively, indicating the high accuracy of ZWD derived from radiosonde data.
 409



410
 411 Figure 11 Uncertainty of ZWD with respect to height at station 01241 (63.70°N/9.60°E/10 m)
 412 at 11:00 UTC on January 1, 2015.

413 Taking the radiosonde ZWDs as reference ZWD values, we validated the ZWDs
 414 from models HZWD, GPT2w and UNB3m. Table 3 shows the statistical results of the
 415 three models. It can be seen from Table 3 that the HZWD model has the best overall
 416 stability of the average bias and RMS error indicating the best precision, and the
 417 UNB3m model is the worst. Compared with the GPT2w model, the RMS errors in
 418 HZWD in the three height intervals are reduced by 0.6 mm, 0.9 mm, and 1.7 mm, which
 419 equates to precision improvements of 2%, 5%, and 33%, respectively. Moreover, these
 420 improvements correspond to an error reduction of 1.2 mm, 1.8 mm, and 3.4 mm
 421 respectively in height estimates in geodetic techniques. Taking the uncertainty of

422 radiosonde ZWD into account, the improvement of HZWD model over GPT2w model
423 below 2 km seem to be insignificant. Nevertheless, we can reasonably think that the
424 ZWD predicted by HZWD is closer to true ZWD due to its smaller RMS error. It is
425 worth noting that the bias and RMS error of the HZWD model and the GPT2w model
426 are both larger than those of the results from ECMWF data in Table 2. The reason is
427 that the HZWD model and the GPT2w model are based on ECMWF data, thus the test
428 results with radiosonde data are slightly worse than those using ECMWF data. On the
429 contrary, the bias of the UNB3m model decreases, and the RMS error between 2 km
430 and 5 km, and 5 km and 10 km, are less than those in Table 2. It may be due to the fact
431 that most of the radiosonde stations are in the northern hemisphere, accounting for more
432 than 60% (192/318) of the total, which has a positive impact on the test results for
433 UNB3m model based on North American meteorological data.

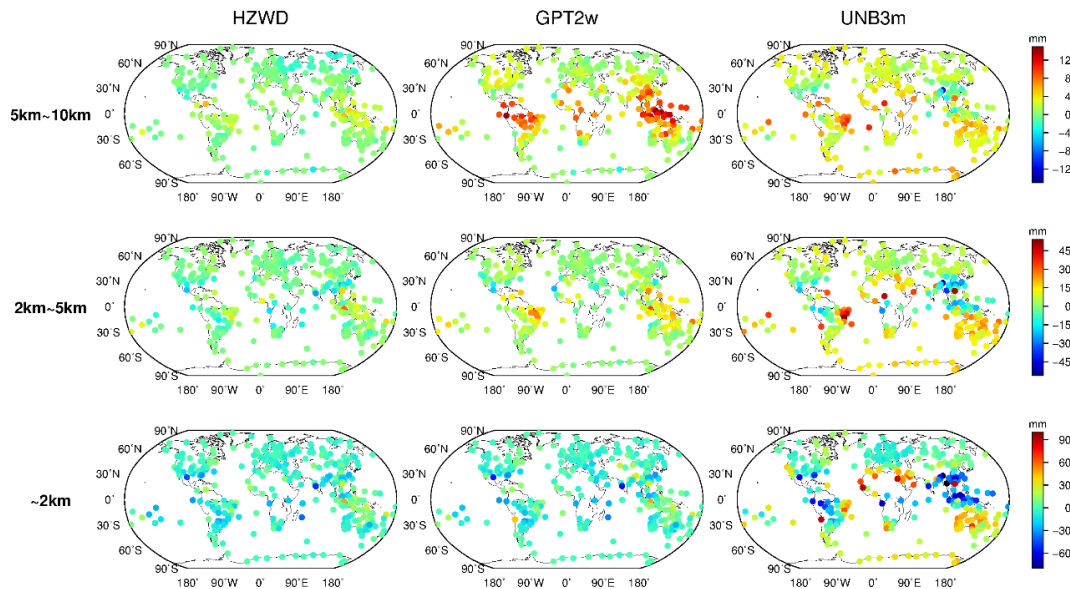
434 Figure 12 shows the global distributions of bias for the three models within the
435 three height intervals, and Figure 13 shows the global distributions of RMS error for
436 the three models. As can be seen from Figure 12, the three models show a poorer
437 performance in low-latitude areas than in mid- and high-latitude areas for all height
438 intervals, similar to the results of in Section 4.1. Within the 5 km to 10 km interval, the
439 bias of the GPT2w model is large and positive in the equatorial region, indicating that
440 the ZWD of the GPT2w in this height is significantly overestimated, and the global bias
441 of the UNB3m model in this height interval is positive, also indicating an overestimate
442 of the ZWD in the UNB3m model. The bias of the HZWD model does not show obvious
443 regional differences with respect to height, and the overall distribution of HZWD model
444 bias has no tendency to either the positive or negative. Figure 13 further illustrates the
445 precision of the HZWD model. The global RMS error distributions of HZWD model
446 are similar to that of GPT2w model below 2 km and between 2 km and 5 km, but the
447 precision of the HZWD model is slightly better. Combining this with the bias
448 distribution of the GPT2w model in Figure 12, the GPT2w model also has a large RMS
449 error near the equator in the 5 km to 10 km interval, which shows that the GPT2w model
450 is unstable at high height in low-latitude areas. The precision of the UNB3m model is
451 poorer than that of both the HZWD, and GPT2w, models. Below 2 km, the UNB3m

452 model reaches decimetre-level precision near the equator, and even exceeds 12 cm in
 453 some areas: the distribution of north-south heterogeneity remains obvious.

454 Table 3 Error statistics for the three models validated by 2015 radiosonde data (unit: mm).

	< 2 km		2 km to 5 km		5 km to 10 km	
	bias	RMS	bias	RMS	bias	RMS
HZWD	-3.6	30.1	-2.0	15.8	0.1	3.5
GPT2w	-3.2	30.7	3.5	16.7	3.3	5.2
UNB3m	5.9	46.0	6.2	23.1	2.6	5.7

455

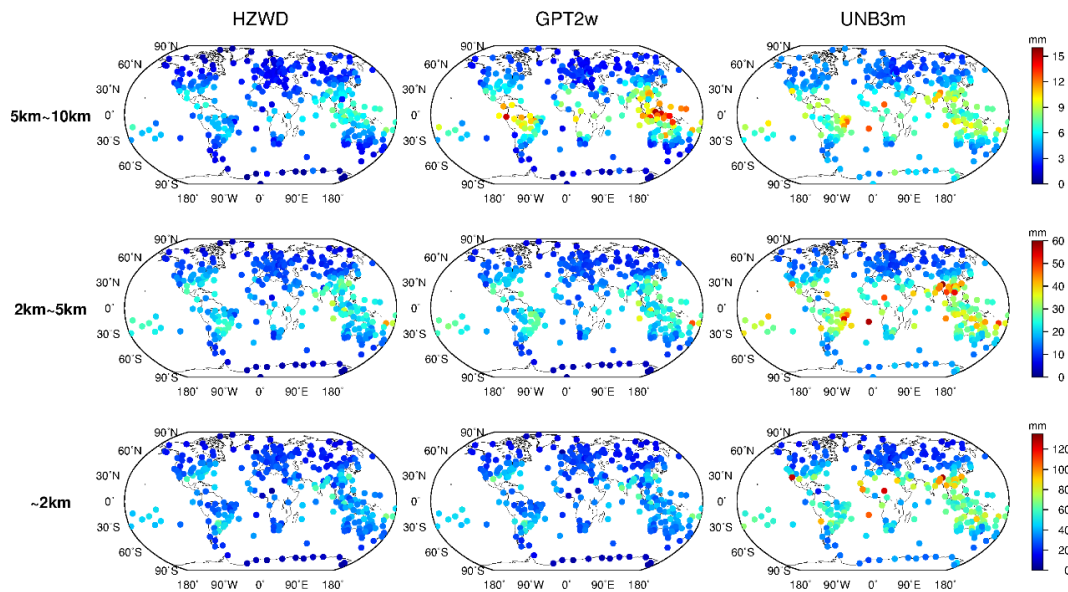


456

457 Figure 12 Global distributions of bias for the three models (HZWD, GPT2w, and UNB3m)

458

compared to 2015 radiosonde data.

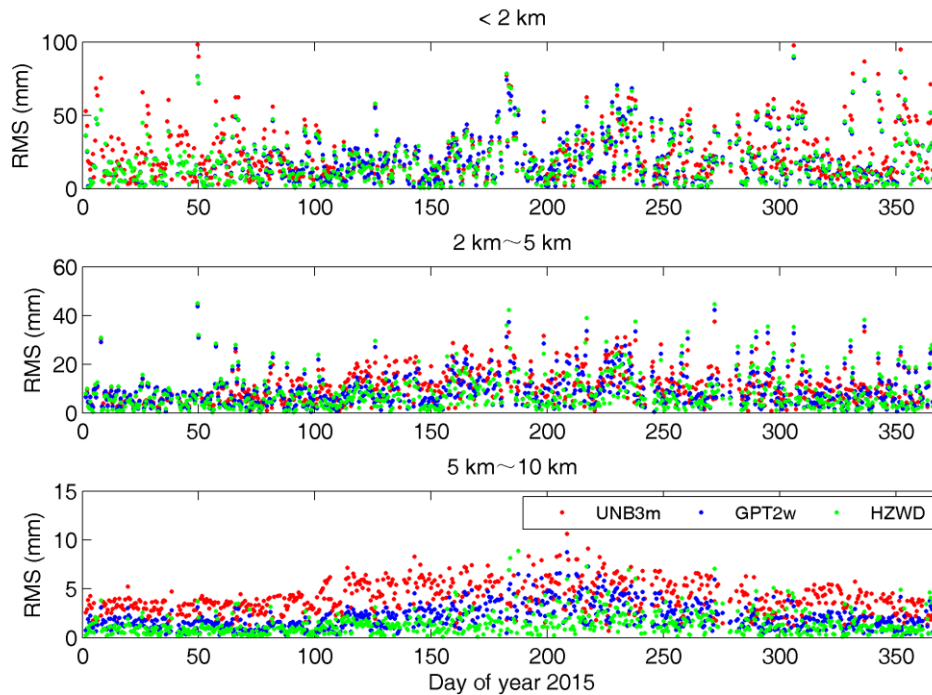


459

460 Figure 13 Global distributions of RMS error for the three models (HZWD, GPT2w, and UNB3m)
 461 compared to 2015 radiosonde data.

462 These results validate the spatial stability of the precision of the HZWD model,
 463 furthermore the temporal stability of the model precision is verified next. Figure 14
 464 shows the results of ZWD corrections of the three models for the radiosonde station
 465 01241 for the whole of 2015. It can be seen from Figure 14 that the HZWD model and
 466 the GPT2w model are relatively stable throughout the year, while the correction
 467 performance of the UNB3m model in 2015 is worse than those of the HZWD and
 468 GPT2w models. The probable reason for this is that the UNB3m model only takes into
 469 account the annual variations in the metrological elements with a fixed phase, resulting
 470 in precision instability throughout the year. The improvement performance arising from
 471 use of the HZWD model, compared to that arising from use of the GPT2w model, is
 472 more apparent with increasing height: this shows that modelling ZWD piecewise with
 473 height can effectively approximate the real ZWD profile and improve the precision of
 474 ZWD estimation.

475



476

477 Figure 14 RMS errors in ZWD estimates of the three models (HZWD, GPT2w, and UNB3m)

478

for radiosonde station 01241 over the year 2015.

479

480 5 Conclusions

481

482

483

484

485

486

487

488

489

490

491

492

493

The complexity of spatio-temporal variations makes the modelling of tropospheric ZWD difficult. In this paper, the characteristics of vertical variation of wet delay are analysed. The troposphere is divided into three height intervals: below 2 km, 2 km to 5 km, and 5 km to 10 km according to different trends (10 km is assumed to represent the empirical tropopause). A quadratic polynomial and two exponential functions are used to describe the variation of wet delay within each of the three intervals. Based on the monthly mean data of ECMWF ZWD from 2001 to 2010, a global ZWD model with spatial resolution of $5^\circ \times 5^\circ$ was established with height fitting followed by periodic fitting. Using the ECMWF ZWD data for 2015, the annual average RMS errors in the HZWD model are 23.8 mm, 13.1 mm, and 2.6 mm in the below 2 km, 2 km to 5 km, and 5 km to 10 km height intervals, respectively, which is far superior to the performance of the UNB3m model. Compared to the currently most accurate wet delay empirical model (the GPT2w model), the precisions within the three height intervals

494 improved by 6% (1.4 mm), 6% (0.9 mm), and 32% (1.2 mm), respectively. The
495 improvements will result in precision improvements of 2.8 mm, 1.8 mm, and 2.4 mm
496 respectively in height estimates in real-time aircraft positioning. The testing results of
497 radiosonde data from 318 stations in 2015 show that the annual average RMS errors of
498 the HZWD model are 30.1 mm, 15.8 mm, and 3.5 mm, which are 2% (0.6 mm), 5%
499 (0.9 mm), and 33% (1.7 mm) better than those of the GPT2w model, respectively,
500 corresponding to height error reduction of 1.2 mm, 1.8 mm, and 3.4 mm in real-time
501 aircraft positioning. Considering the ZWD fields (0.126 m, 0.0489 m, and 0.0111 m) in
502 the three height intervals, the precision improvements at the top layer are especially
503 significant, which accounts for about 15% of the corresponding ZWD field. Moreover,
504 compared with the GPT2w, and UNB3m, models, the HZWD model offers the highest
505 spatio-temporal stability. With higher precision of ZWD estimates and less model
506 parameters, the HZWD model is more efficient than the GPT2w model.

507 The HZWD model offers good precision stability in the vertical direction and can
508 meet the requirements of ZWD correction at different heights within the troposphere;
509 however, it can be seen that neither the HZWD, nor the GPT2w models, *i.e.*, those non-
510 meteorological parameter-based models, performed well in the lowest region of the
511 troposphere. In addition, compared with GPT2w, HZWD model is a closed model with
512 a limitation to facilitate on-site meteorological observations. Further research is
513 required to assess the variation and factors influencing of the wet delay and explore the
514 possibility of incorporation of on-site meteorological data.

515

516 *Acknowledgements:* The authors would like to thank the ECMWF and IGRA for
517 providing relevant data. We thank the reviewers for their insightful comments and
518 constructive suggestions. This research was supported by the National Key Research
519 and Development Program of China (2016YFB0501803) and the National Natural
520 Science Foundation of China (41574028) and Key Laboratory of Geospace
521 Environment and Geodesy, Ministry of Education, Wuhan University (16-02-03).

522

523 **References**

- 524 Askne, J., & Nordius, H. (1987). Estimation of tropospheric delay for microwaves from surface
525 weather data. *Radio Science*, 22(3), 379-386.
- 526 Bevis, M., Businger, S., Herring, T. A., Rocken, C., Anthes, R. A., & Ware, R. H. (1992). GPS
527 meteorology: Remote sensing of atmospheric water vapor using the Global Positioning System.
528 *Journal of Geophysical Research: Atmospheres*, 97(D14), 15787-15801.
- 529 Bevis, M., Businger, S., Chiswell, S., Herring, T. A., Anthes, R. A., Rocken, C., & Ware, R. H.
530 (1994). GPS meteorology: Mapping zenith wet delays onto precipitable water. *Journal of applied*
531 *meteorology*, 33(3), 379-386.
- 532 B öhm, J., & Schuh, H. (Eds.). (2013). *Atmospheric effects in space geodesy (Vol. 5)*. Berlin:
533 Springer.
- 534 B öhm, J., Möller, G., Schindelegger, M., Pain, G., & Weber, R. (2015). Development of an improved
535 empirical model for slant delays in the troposphere (GPT2w). *GPS Solutions*, 19(3), 433-441.
- 536 Collins, P., Langley, R., & LaMance, J. (1996). Limiting factors in tropospheric propagation delay
537 error modelling for GPS airborne navigation. *Proc. Inst. Navig. 52nd Ann. Meet*, 3.
- 538 Davis, J. L., Herring, T. A., Shapiro, I. I., Rogers, A. E. E., & Elgered, G. (1985). Geodesy by radio
539 interferometry: Effects of atmospheric modeling errors on estimates of baseline length. *Radio*
540 *science*, 20(6), 1593-1607.
- 541 Dee, D. P., Uppala, S. M., Simmons, A. J., Berrisford, P., Poli, P., Kobayashi, S., ... & Bechtold, P.
542 (2011). The ERA - Interim reanalysis: Configuration and performance of the data assimilation
543 system. *Quarterly Journal of the royal meteorological society*, 137(656), 553-597.
- 544 Fernandes, M. J., Nunes, A. L., & L ázaro, C. (2013). Analysis and inter-calibration of wet path
545 delay datasets to compute the wet tropospheric correction for CryoSat-2 over ocean. *Remote*
546 *Sensing*, 5(10), 4977-5005.
- 547 Fernandes, M. J., L ázaro, C., Nunes, A. L., & Scharroo, R. (2014). Atmospheric corrections for
548 altimetry studies over inland water. *Remote Sensing*, 6(6), 4952-4997.
- 549 Hobiger, T., Ichikawa, R., Koyama, Y., & Kondo, T. (2008). Fast and accurate ray - tracing
550 algorithms for real - time space geodetic applications using numerical weather models. *Journal of*
551 *Geophysical Research: Atmospheres*, 113(D20).

552 Hopfield, H. S. (1971). Tropospheric effect on electromagnetically measured range: Prediction from
553 surface weather data. *Radio Science*, 6(3), 357-367.

554 Jin, S., Park, J. U., Cho, J. H., & Park, P. H. (2007). Seasonal variability of GPS - derived zenith
555 tropospheric delay (1994 - 2006) and climate implications. *Journal of Geophysical Research:*
556 *Atmospheres* (1984 - 2012), 112(D9).

557 Kouba, J. (2008). Implementation and testing of the gridded Vienna Mapping Function 1 (VMF1).
558 *Journal of Geodesy*, 82(4-5), 193-205.

559 Krueger, E., Schueler, T., Hein, G. W., Martellucci, A., & Blarzino, G. (2004, May). Galileo
560 tropospheric correction approaches developed within GSTB-V1. In *Proc. ENC-GNSS* (Vol. 1619).

561 Krueger, E., Schueler, T., & Arbesser-Rastburg, B. (2005). The standard tropospheric correction
562 model for the European satellite navigation system Galileo. *Proc. General Assembly URSI*.

563 Lagler, K., Schindelegger, M., Böhmer, J., Krásný H., & Nilsson, T. (2013). GPT2: Empirical slant
564 delay model for radio space geodetic techniques. *Geophysical research letters*, 40(6), 1069-1073.

565 Leandro, R., Santos, M. C., & Langley, R. B. (2006, January). UNB neutral atmosphere models:
566 development and performance. In *Proceedings of ION NTM* (Vol. 52, No. 1, pp. 564-73).

567 Müller, G., Weber, R., & Böhmer, J. (2014). Improved troposphere blind models based on numerical
568 weather data. *Navigation*, 61(3), 203-211.

569 Nafisi, V., Madzak, M., Böhmer, J., Ardalan, A. A., & Schuh, H. (2012). Ray-traced tropospheric
570 delays in VLBI analysis. *Radio Science*, 47(02), 1-17.

571 Niell, A. E. (1996). Global mapping functions for the atmosphere delay at radio wavelengths.
572 *Journal of Geophysical Research: Solid Earth*, 101(B2), 3227-3246.

573 Nilsson, T., & Elgered, G. (2008). Long - term trends in the atmospheric water vapor content
574 estimated from ground - based GPS data. *Journal of Geophysical Research: Atmospheres*,
575 113(D19).

576 Rózsa S.Z. Uncertainty considerations for the comparison of water vapour derived from radiosondes
577 and GNSS[M]/Earth on the Edge: Science for a Sustainable Planet. Springer Berlin Heidelberg,
578 2014: 65-78.

579 RTCA (2016), Minimum Operational Performance Standards For Global Positioning
580 System/Satellite-Based Augmentation System Airborne Equipment, Radio Technical Commission
581 for Aeronautics, SC-159, publication DO-229E, Washington, D. C.

582 Saastamoinen, J. (1972). Introduction to practical computation of astronomical refraction. *Bulletin*
583 *G ód é sique* (1946-1975), 106(1), 383-397.

584 Sch ¨ u l e r, T. (2014). The TropGrid2 standard tropospheric correction model. *GPS solutions*, 18(1),
585 123-131.

586 Song, S., Zhu, W., Chen, Q., & Liou, Y. (2011). Establishment of a new tropospheric delay
587 correction model over China area. *Science China Physics, Mechanics and Astronomy*, 54(12), 2271-
588 2283.

589 Stum, J., Sicard, P., Carrere, L., & Lambin, J. (2011). Using objective analysis of scanning
590 radiometer measurements to compute the water vapor path delay for altimetry. *IEEE Transactions*
591 *on Geoscience and Remote Sensing*, 49(9), 3211-3224.

592 Vieira, T., Fernandes, M. J., & L á z a r o, C. (2018). Analysis and retrieval of tropospheric corrections
593 for cryosat-2 over inland waters. *Advances in Space Research*, 62(6), 1479-1496.

594 Zhao J Y, Song S L, Chen Q M, et al. (2014). Establishment of a new global model for zenith
595 tropospheric delay based on functional expression for its vertical profile. *Chinese J. Geophys.* (in
596 Chinese), 57(10), 3140-3153.

597